Non-Kramers ESEEM of Integer-Spin Diferrous Carboxylate-Bridged Clusters in Proteins

Bradley E. Sturgeon,[†] Peter E. Doan,[†] Katherine E. Liu,[‡] Doug Burdi,[‡] Wing H. Tong,[‡] Judith M. Nocek,[†] Nishi Gupta,[§] JoAnne Stubbe,[‡] Donald M. Kurtz, Jr.,[§] Stephen J. Lippard,[‡] and Brian M. Hoffman*,[†]

Contribution from the Department of Chemistry, Northwestern University, 2145 Sheridan Road, Evanston, Illinois 60208-3113, Department of Chemistry, Massachusetts Institute of Technology, Cambridge, Massachusetts 02139, and Department of Chemistry and Center for Metalloenzyme Studies, University of Georgia, Athens, Georgia 30602-2556

Received August 12, 1996[⊗]

Abstract: The diferrous oxidation level of carboxylate-bridged non-heme diiron proteins is pivotal because only it reacts directly with dioxygen. In this state each ferrous ion has $S_T = 2$. Such integer-spin, so-called "Non-Kramers" (NK) systems typically are difficult to access by paramagnetic resonance techniques, and this property has precluded the application of ENDOR and ESEEM spectroscopies to this state. Integer-spin systems frequently exhibit a ground state "Non-Kramers doublet", however, which is split in zero applied field by an energy within the microwave range, thus rendering the center EPR active. Recently, we showed that ENDOR and ESEEM spectroscopies also can be applied to NK doublets, in preliminary measurements on diferrous methane monooxygenase hydroxylases (MMOH$_{red}$) *Methylococcus capsulatus* (Bath) and *Methylosinus trichosporium* OB3b and azido-hemerythrin (N$_3$-Hr$_{red}$) (Hoffman, B. M.; Sturgeon, B. E.; Doan, P. E.; DeRose, V. J.; Liu, K. E.; Lippard, S. J. *J. Am. Chem. Soc.* **1994**, *116*, 6023−6024). Building on this study plus subsequent theoretical work (Hoffman, B. M. *J. Phys. Chem.* **1994**, *98*, 11657−11665), we now present a comparative 3-pulse ESEEM study of the diiron(II) centers of the two MMOH$_{red}$, N$_3$Hr$_{red}$, N$_3$Ribonucleotide reductase (N$_3$R2$_{red}$), N$_3$Rubrerythrin (N$_3$Rr$_{red}$), and N$_3$-"Chopped" Rubrerythrin (N$_3$CRr$_{red}$), which lacks the 39-residue C-terminal FeS$_4$ domain. This report first presents the theory necessary for quantitative interpretations of the frequency-domain (ENDOR-like) spectra obtained by three-pulsed ESEEM measurements performed in the limit where the external magnetic field (B_o) oriented parallel to the microwave field is small: $B_o \lesssim 20$ G. It then presents experimental NK-ESEEM results for ^{14}N nuclei from coordinated histidine of each of the five diferrous proteins and from azide of the three azido-proteins. The measurements yield ^{14}N quadrupole tensors to high precision as well as estimates of hyperfine couplings. In addition they provide otherwise unavailable information about the orientations of the tetragonal crystal fields of the individual ferrous ions. The data suggest that the histidyl ligands to the cluster play a major role in determining the electronic structure of the functionally important diferrous state of these proteins. They disclose a surprising reorientation of azide in the Rr$_{red}$ pocket upon deletion of the C-terminal domain.

Carboxylate-bridged non-heme diiron proteins have similar structural cores while performing diverse reactions with dioxygen, including O$_2$ binding (hemerythrin (Hr)) and activation (ribonucleotide reductase (R2), methane monooxygenase (MMOH), and rubrerythrin (Rr)).[1−3] The diferrous form of these proteins is pivotal because only it reacts directly with dioxygen. In this state each ferrous ion has a spin of $S_T = 2$,[4,5] and such integer-spin, so-called "Non-Kramers" (NK), systems typically are difficult to access by paramagnetic resonance techniques. It has been known for over forty years, however, that systems with integer total angular momentum of 2 or greater and an appropriate type of near-axial zero-field splitting (ZFS) can exhibit a "Non-Kramers doublet" that is split in zero applied field by an energy within the microwave range, which leaves the center EPR active.[6−9] Protein-bound, carboxylate-bridged diiron(II) centers frequently display the characteristic EPR spectrum associated with a ground-state non-Kramers doublet, which has facilitated extensive EPR studies of these systems and brought about a resurgence of interest in integer-spin EPR spectroscopy.[4,10−12] More recently, a preliminary study[13] of MMOH$_{red}$ from two sources and of N$_3$Hr$_{red}$ demonstrated that NK doublets also can be studied by ENDOR and ESEEM spectroscopies, which have provided profound insights into the

---

* Author to whom correspondence should be addressed.
† Northwestern University.
‡ Massachusetts Institute of Technology.
§ University of Georgia.
⊗ Abstract published in *Advance ACS Abstracts,* December 15, 1996.

(1) Abbreviations: NK, non-Kramers; ENDOR, electron nuclear double resonance; ESEEM, electron spin echo envelope modulation; ZFS, zero-field splitting; MMOH, hydroxylase component of methane monooxygenase: unless specified otherwise, hydroxylase is from *Methylococcus capsulatus* (Bath) (*Mc*); data for hydroxylase from *Methylosinus trichosporium* OB3b (*Mt*) also are presented; Hr, hemerythrin; Rr and CRr, rubrerythrin and the genetically engineered form with the 39-residue C-terminal FeS$_4$ domain deleted; R2, ribonucleotide reductase R2 protein.

(2) Kurtz, D. M., Jr. *Encyclopedia of Inorganic Chemistry*; King, R. B., Ed.; Wiley: U.K., 1994; pp 1847−1859.

(3) Que, L. J.; Dong, Y. *Acc. Chem. Res.* **1996**, *29*, 190−196.

(4) Hendrich, M. P.; Pearce, L. L.; Que, L., Jr.; Chasteen, N. D.; Day, E. P. *J. Am. Chem. Soc.* **1991**, *113*, 3039−3044.

(5) Reem, R. C.; Solomon, E. I. *J. Am. Chem. Soc.* **1987**, *109*, 1216−1226.

(6) Bleaney, B.; Scovil, H. E. D. *Philos. Mag.* **1952**, *43*, 999−1000.

(7) Tinkham, M. *Proc. R. Soc. London* **1956**, *A236*, 535−548.

(8) Baker, J. M.; Bleaney, B. *Proc. R. Soc. London* **1958**, *A245*, 156−174.

(9) Griffith, J. S. *Phys. Rev.* **1963**, *132*, 316−319.

(10) Hendrich, M. P.; Debrunner, P. G. *Biophys. J.* **1989**, *56*, 489−506.

(11) Münck, E.; Surerus, K.; Hendrich, M. P. *Methods Enzymol., Part C* **1993**, *227*, 463−479.

(12) Hendrich, M. P.; Münck, E.; Fox, B. G.; Lipscomb, J. D. *J. Am. Chem. Soc.* **1990**, *112*, 5861−5865.

(13) Hoffman, B. M.; Sturgeon, B. E.; Doan, P. E.; DeRose, V. J.; Liu, K. E.; Lippard, S. J. *J. Am. Chem. Soc.* **1994**, *116*, 6023−6024.

composition, geometric, and electronic structure of ordinary half-integer (Kramers) spin systems[14-16] including the mixed-valence states of these dinuclear centers.[17] Building on this discovery and a subsequent theoretical investigation,[18] we now present a comparative 3-pulse ESEEM[19,20] study of the diiron(II) centers of N_3Hr_{red}, N_3R2_{red}, the two $MMOH_{red}$,[1] N_3Rr_{red}, and N_3CRr_{red}, where CRr lacks the 39-residue C-terminal domain of Rr.[21]

These proteins are ideal for a comparative spectroscopic investigation because they contain very similar diiron clusters, yet exhibit clear variations in function. The structures of the diferric proteins have been solved by X-ray crystallography,[1,22-26] as have the diferrous forms of the first three.[22,24,26,27] The structures show noticeable differences, as indicated in Figure 1. The diferrous centers of R2 and MMOH each exhibit two bridging carboxylates, along with terminal coordination to each Fe^{II} of one additional carboxylate and one histidine. However, the diferrous center in $MMOH_{red}$ has two weakly coordinated water molecules, one of them acting as a semibridge between the two Fe^{II} ions, whereas $R2_{red}$ has two four-coordinate Fe^{II} ions and no bound water or other exogenous Fe ligands. The structure of diferric Rr has only one coordinated histidine and five rather than four carboxylate ligands, two of which are bridging, along with an oxo-bridge. Hr_{red} has one five-coordinate and one six-coordinate Fe^{II} ion, with two bridging carboxylates and a hydroxo bridge; there are no terminal carboxylates, but five histidyl ligands instead. Oxy-Hr is formed by addition of the O_2 moiety to the five-coordinate iron ion. The diferrous centers of Hr, R2, and Rr(CRr) do not display NK-EPR signals, but they bind azide to give EPR-active NK spin signals.[4,21,28] The structures of these adducts have not been determined by X-ray crystallography.

In the present article we first develop the general theory[18] to permit quantitative interpretations of the frequency-domain (ENDOR-like) spectra obtained by ESEEM measurements on NK systems performed with low applied magnetic fields, $0 < B_o \lesssim 20$ G. We next present extensive experimental NK-ESEEM results for ^{14}N nuclei of coordinating histidines of each of the diferrous proteins and from the azide nitrogen for those where azide coordination is required to generate a NK doublet. Our results suggest that the histidine ligands play a key role in
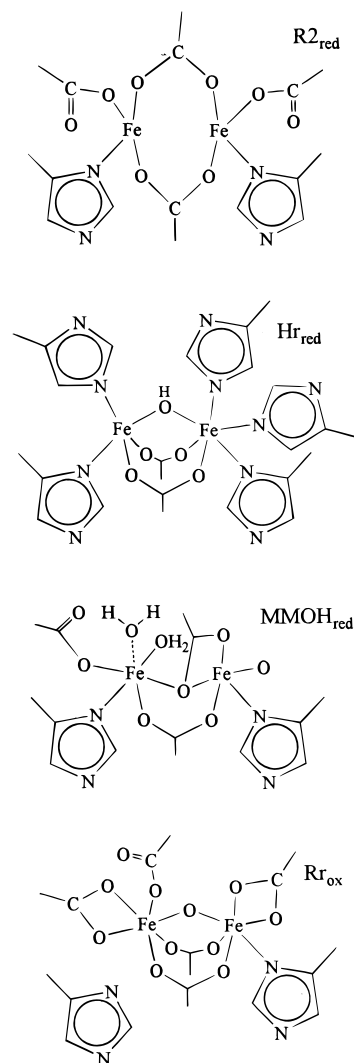

Figure 1. Structures of carboxylate-bridged diiron(II) centers.

controlling the electronic structure of the functionally important diferrous state. Azide binding may mimic that of dioxygen, and the present findings indicate that bound azide is a sensitive probe of conformational perturbations at the cluster.

Materials and Methods

Preparation of N_3Hr_{red}. Hr was isolated from *Phascolopsis gouldii* according to the standard procedure described by Klotz *et al.*[29] Crystals of the fully oxidized form of Hr (Hr_{ox}) were dissolved in 50 mM sodium phosphate buffer (pH 6.5) containing 0.2 M sodium sulfate (Na_2SO_4) to make an ≈4 mM protein solution ($\epsilon_{500} = 2.2$ mM^{-1} cm^{-1}).[30] The reduced form of Hr (Hr_{red}) was prepared according to the procedure described by Nocek *et al.*[31] A solution of Hr_{ox} was dialyzed anaerobically at 4 °C against 10 mM sodium dithionite ($Na_2S_2O_4$) for ≈18 h. Excess sodium dithionite was then removed by anaerobic dialysis against several changes of buffer solution. Solutions of Hr_{red} were transferred anaerobically from the dialysis bag into a 25-mL Schlenk flask attached to the vacuum manifold via the side-arm stopcock. A 25-μL aliquot of a 2 M deoxygenated, stock solution of either sodium azide (NaN$_3$) or triply ^{15}N-labeled sodium azide (Na^{15}N$_3$) (99% ^{15}N, Cambridge Isotope Laboratories, Andover, MA) was added with a gas tight syringe to a 250-μL aliquot of Hr_{red} under a nitrogen

(14) Hoffman, B. M.; DeRose, V. J.; Doan, P. E.; Gurbiel, R. J.; Houseman, A. L. P.; Telser, J. In *EMR of Paramagnetic Molecules*; Biological Magnetic Resonance 13; Berliner, L. J., Reuben, J., Eds.; Plenum Press: New York, 1993; pp 151−218.

(15) DeRose, V. J.; Hoffman, B. M. In *Methods Enzymol.* **1995**, *246*, 555−589.

(16) Lowe, D. J. *ENDOR and EPR of Metalloproteins*; R. G. Landes Co.: Austin, TX, 1995.

(17) DeRose, V. J.; Liu, K. E.; Lippard, S. J.; Hoffman, B. M. *J. Am. Chem. Soc.* **1996**, *118*, 121−134.

(18) Hoffman, B. M. *J. Phys. Chem.* **1994**, *98*, 11657−11665.

(19) Mims, W. B. In *Electron Paramagnetic Resonance*; Geschwind, S., Ed.; Plenum Press: New York, 1972; pp 263−351.

(20) Bowman, M. K.; Massoth, R. J. In *Electronic Magnetic Resonance of the Solid State*; Weil, J. A., Ed.; The Canadian Society for Chemistry: Ottawa, 1987; pp 99−110.

(21) Gupta, N.; Bonomi, F.; Kurtz, D. M., Jr.; Ravi, N.; Wang, D. L.; Huynh, B. H. *Biochemistry* **1995**, *34*, 3310−3318.

(22) deMaré, F.; Kurtz, D. M., Jr.; Nordlund, P. *Nature Struct. Biol.* **1996**, *3*, 539−546.

(23) Stenkamp, R. E. *Chem. Rev.* **1994**, *94*, 715−726.

(24) Rosenzweig, A. C.; Nordlund, P.; Takahara, P. M.; Frederick, C. A.; Lippard, S. J. *Chem. Biol.* **1995**, *2*, 409−418.

(25) Rosenzweig, A. C.; Frederick, C. A.; Lippard, S. J.; Nordlund, P. *Nature* **1993**, *115*, 939−947.

(26) Nordlund, P.; Eklund, H. *Curr. Opin. Struct. Biol.* **1995**, *5*, 758−766.

(27) (a) Feig, A. L.; Lippard, S. J. *Chem. Rev.* **1994**, *94*, 759−805. (b) Que, L.; True, A. E. In *Progress in Inorganic Chemistry*; Lippard, S. J., Ed.; John Wiley & Sons: New York, 1990; pp 201−258.

(28) Elgren, T. E.; Hendrian, M. P.; Que, L. *J. Am. Chem. Soc.* **1993**, *115*, 9291−9292.

(29) Klotz, I. M.; Klotz, T. A.; Fiess, H. A. *Arch. Biochem. Biophys.* **1957**, *68*, 284−289.

(30) Garbett, K.; Darnell, D. W.; Klotz, I. M.; Williams, R. J. P. *Arch. Biochem. Biophys.* **1971**, *142*, 574−583.

(31) Nocek, J. M.; Kurtz, D. M., Jr.; Sage, J. T.; Xia, Y.; DeBrunner, P.; Shiemke, A. K.; Sanders-Loehr, J.; Loehr, T. M. *Biochemistry* **1988**, *27*, 1014−1024.

blanket. Samples (60-μL) of N_3Hr_{red} were transferred into a 2.0 mm i.d. fused silica tube and immediately frozen in liquid nitrogen. The concentration of Hr_{red} was determined by exposing a sample to air in the absence of NaN_3 and measuring the optical spectrum of the Hr_{ox} with a Hewlett-Packard diode array spectrophotometer.

Preparation of $MMOH_{red}$. Growth of native *M. capsulatus* (Bath) and purification of hydroxylase and protein B were carried out as described elsewhere.[32,33] Specific activities and iron content were in the ranges reported. Growth of *M. trichosporium* OB3b and purification of its hydroxylase were performed as described.[34] The specific activity of the *M. trichosporium* OB3b hydroxylase for the conversion of propylene to propylene oxide was monitored with the use of protein B and reductase from *M. capsulatus* (Bath). *M. capsulatus* (Bath) cells were grown in an ^{15}N enriched medium[35] in order to obtain correspondingly ^{15}N-enriched hydroxylase samples. The usual media for fermentations was altered only in that KNO_3 (99% ^{15}N, Cambridge Isotope Laboratories) was used.

To prepare samples for ENDOR measurements, ~50 mg of hydroxylase was concentrated to a volume of 2 mL at 4000 rpm by using Centriprep centrifugal concentrators (Amicon) with a molecular weight cutoff of 30 000. The 2-mL concentrates were then placed in Centricon concentrators (Amicon) with the same molecular weight cutoff. The sample volume was decreased to $\approx$100 μL, resulting in a concentration of at least 1 mM. A small volume of a stock solution of 10 mM methyl viologen was added to achieve a 1 mM concentration in the sample. The solution was placed in a vial, sealed with a septum, and then made anaerobic by repeatedly evacuating and back-filling with dioxygen-free argon. To reduce each batch, a small volume of a 0.1 M solution of sodium dithionite was added to achieve a concentration of $\approx$2 mM sodium dithionite in the sample. The solutions were allowed to equilibrate for 30 min and were simultaneously brought into an anaerobic chamber (Vacuum Atmospheres). The samples were then loaded into the appropriate tubes, capped with a septum, brought out of the box, and immediately frozen in liquid N_2.

Preparation of N_3Rr_{red}(N_3CRr_{red}). Recombinant *Desulfovibrio vulgaris* Rr (CRr) was prepared by the procedure of Gupta *et al.*[21] The concentration of the oxidized Rr (Rr_{ox}) was determined by using a homodimer extinction coefficient $\epsilon_{492} = 10.6$ mM^{-1} cm^{-1}.[36] The fully reduced form of Rr (Rr_{red}) was prepared by adding a 10-μL aliquot of a standardized solution of 100 mM sodium dithionite ($Na_2S_2O_4$) to a 75-μL aliquot of a 1 mM (homodimer) solution of Rr_{ox} in 50 mM HEPES buffer (pH 7) containing 0.2 M sodium sulfate. Solutions of sodium dithionite were standardized by reaction with a standard solution of $K_3Fe(CN)_6$ ($\epsilon_{419} = 1030$ mM^{-1} cm^{-1}).[37] Addition of a 10-fold molar excess of sodium dithionite bleached the color of the sample within 5 min, indicating the complete reduction of both the dinuclear iron site and the rubredoxin site. Subsequent to reduction, a 10-μL aliquot of 1 M stock solutions of either sodium azide (NaN_3) or triply ^{15}N-labeled sodium azide ($Na^{15}N_3$) (99% ^{15}N, Cambridge Isotope Laboratories) was added with a gas tight syringe to the 75-μL aliquot of Rr_{red}. Samples (60-μL) of N_3Rr_{red} were transferred into 2.0 mm i.d. fused silica tubes and immediately frozen in liquid nitrogen. N_3CRr_{red} was prepared similarly using $\hat{\epsilon}_{365} = 12.0$ mM^{-1} cm^{-1} for CRr_{ox} homodimer.[21]

Preparation of *apo*-R2. Wild-type protein R2, containing both stable tyrosyl radical and diferric cluster, was isolated from the overproducing strain N6405/pSPS2 as previously reported.[38] *apo*-R2 was prepared from the wild-type precursor via a modification[39] of the chelation procedure of Atkin *et al.*[40] Concentrations of *apo*-R2 were

determined by absorbance at 280 nm according to the published[41] molar absorption coefficient ($\epsilon_{280} = 120$ mM^{-1} cm^{-1}).

Preparation of N_3R2_{red}. $R2_{red}$ can bind one or two azide ions, depending on conditions.[28,42] The samples studied here were prepared under the conditions that produce protein with one bound azide. A solution of 0.614 mM *apo*-R2 in 100 mM HEPES buffered at pH 7.6 was gently deoxygenated on a gas train by briefly applying a vacuum and reintroducing argon gas. This cycle was repeated three times. In a separate flask, an aqueous solution of 6 mM sodium dithionite (Na_2SO_4) and either sodium azide (NaN_3) or triply ^{15}N-labeled sodium azide ($Na^{15}N_3$) (99% ^{15}N, Cambridge Isotope Laboratories) (420 mM) was prepared and deoxygenated using the same repeat cycles of evacuation and argon saturation. $FeSO_4 \cdot 7H_2O$ (17 mg, 61 μmol) was added to a third flask containing 5 mN H_2SO_4 (5 mL), deoxygenated, and saturated with argon. These three solutions were sealed and transferred, along with sample tubes, into an anaerobic glovebox. In a 1-mL Eppendorf tube were combined *apo*-R2 solution, sodium azide/dithionite solution, and $FeSO_4$ solution. The final composition of the resulting protein solution was 511 μM *apo*-R2, 67 mM HEPES at pH 7.6, 2.03 mM Fe^{2+}, 70 mM NaN_3, and 1 mM sodium dithionite. The final composition of the triply ^{15}N-labeled sodium azide containing protein solution was 383 μM *apo*-R2, 67 mM HEPES at pH 7.6, 1.53 mM Fe^{2+}, 70 mM $Na^{15}N_3$, and 1 mM sodium dithionite. Samples (60-μL) of N_3-$R2_{red}$ were transferred into 2.0 mm i.d. fused silica tubes and sealed tightly in cryotubes before removal from the glovebox. Upon removal from the glovebox, these samples were immediately frozen in liquid nitrogen.

ESEEM. ESEEM experiments were carried out on a laboratory-built spectrometer described elsewhere.[43] The liquid helium dewar was remounted outside of the standard EPR magnet, in order to position a pair of Helmholz coils around the dewar tail. The Helmholz coils were constructed to allow either perpendicular or parallel orientation to the B_1 field produced by the microwave radiation. The magnetic field was measured using a F. W. Bell, model 4048 gaussmeter.

ESEEM time waves were collected using a standard three-pulse stimulated echo sequence.[19,20] Two-pulse experiments were performed, but very short phase memories (T_m) (<500 ns) limited the information obtained. Data were collected for parallel magnetic fields of less than 14 G, under a set of standard experimental conditions: microwave pulse widths of 16 ns; $\tau = 140$ ns; T incremented in 256 pts/scan, with 40 ns steps, beginning at $T = 140$ ns; temperature of 2 K, 100 Hz repetition rate. Data averaging varied with sample: 500, 1500, 2760, and 1500 transients/pt for Hr_{red}, $MMOH_{red}$, $R2_{red}$, and Rr_{red}, respectively. The frequency-domain spectra were produced using the deadtime reconstruction method of Mims before Fourier transformation;[44] the time waves for N_3Hr_{red} and $N_3(C)Rr_{red}$ were apodized.

A program has been written that calculates statistical NK ESEEM (frequency-domain) powder spectra and time-domain traces. Mims' density-matrix treatment for ESEEM[20] holds for NK,[18] as well as Kramers, systems. The theory's equation for the amplitude of the stimulated echo produced by a series of three $\pi/2$ pulses, ($\pi/2-\tau-\pi/2-T-\pi/2$), denoted $\epsilon(\tau,T)$, is written in terms of the matrix M that maps the nuclear eigenvectors of one electron-spin m_s level onto those of the other.[19,20] The exact eigenvalues and eigenvectors of $\hat{H}_{nuc}(m_s)$ (eq 8), as obtained from the expressions of Muha,[45] are used in calculations of the frequency-dependent amplitude-modulation function $\epsilon(\tau,T)$.[20] The ESEEM frequency-domain statistical powder spectrum for a NK doublet is obtained directly in the absence of line broadening by generating a histogram, modulation depth *vs* frequency, using a uniform distribution, $p(B_z) = 1/B_o$. This choice of distribution is justified by the fact that Δ for a NK doublet is distributed, and thus for any applied field, B_o, the resonance condition will be satisfied by molecules of every orientation (θ), because for each θ there are molecules that exhibit a value of Δ which satisfies the resonance

(32) DeWitt, J. G.; Bentsen, J. G.; Rosenzweig, A. C.; Hedman, B.; Green, J.; Pilkington, S.; Papaefthymiou, G. C.; Dalton, H.; Hodgson, K. O.; Lippard, S. J. *J. Am. Chem. Soc.* **1991**, *113*, 9219−9235.

(33) Liu, K. E.; Johnson, C. C.; Newcomb, M.; Lippard, S. J. *J. Am. Chem. Soc.* **1993**, *115*, 939−947.

(34) Fox, B. G.; Froland, W. A.; Jollie, D. R.; Lipscomb, J. D. *Methods In Enzymology*; Academic Press: New York, 1990; pp 191−202.

(35) Pilkington, S. J.; Dalton, H. In *Methods in Enzymology*; Academic Press: New York, 1990; pp 181−190.

(36) Ravi, N.; Prickril, B. C.; Kurtz, D. M., Jr.; Huynh, B. H. *Biochemistry* **1993**, *32*, 8487−8491.

(37) Irwin, M. J.; Duff, L. L.; Shriver, D. F.; Klotz, I. M. *Arch. Biochem. Biophys.* **1983**, *224*, 473−478.

(38) Salowe, S. P.; Stubbe, J. *J. Bacteriology* **1986**, *165*, 363−366.

(39) Salowe, S. P. Ph.D. Thesis, University of Wisconsin, 1987.

(40) Atkin, C. L.; Thelander, L.; Reichard, P.; Lang, G. *J. Biol. Chem.* **1973**, *248*, 7464−7472.

(41) Thelander, L. *J. Biol. Chem.* **1973**, *248*, 4591−4601.

(42) Pulver, S. C.; Tong, W. H.; Bollinger, J. M.; Stubbe, J.; Solomon, E. T. *J. Am. Chem. Soc.* **1995**, *119*, 12,664−12,678.

(43) Fan, C.; Doan, P. E.; Davoust, C. E.; Hoffman, B. M. *J. Magn. Reson.* **1992**, *98*, 62−72.

(44) Mims, W. B. *J. Magn. Reson.* **1984**, *59*, 291−306.

(45) Muha, G. M. *J. Magn. Reson.* **1982**, *49*, 431−443.

condition such that ν_e (eq 3) = ν_m. The distribution for Δ[10,11] is far broader than the band of spins excited by a microwave pulse, and so the distribution function may be taken as uniform. Each histogram was calculated by a simple summation of 500 field points evenly distributed between 0 and B_o, normalized so that $\epsilon(\tau=0,T=0) \equiv 1$. Line broadening is modeled by convolving a histogram with a Gaussian component line shape in the frequency domain.

NK ESEEM of Diiron Centers

The ground electronic state of two magnetically coupled (J) high-spin iron(II) ions ($S_T = 2$) in an applied field (B_o) is described by the spin Hamiltonian given by eq 1. In a typical

$$\hat{H} = \hat{S}_1 \cdot \mathbf{D}_1 \cdot \hat{S}_1 + \hat{S}_2 \cdot \mathbf{D}_2 \cdot \hat{S}_2 + J\hat{S}_1 \cdot \hat{S}_2 + \\ \beta(\hat{S}_1 \cdot \mathbf{g}_1 + \hat{S}_2 \cdot \mathbf{g}_2) \cdot B_o + \sum_{ij} \hat{S}_i \cdot \mathbf{A}_{ij} \cdot \hat{I}_j \quad (1)$$

diferrous carboxylate-bridged center each ferrous ion experiences a strong tetragonal crystal field. This leads to a ZFS interaction tensor ($\mathbf{D}_i$, $i = 1, 2$) that exhibits a dominant tetragonal component (D_i, $= 3D_{zzi}/2$) along the axis of the tetragonal distortion, denoted z_i. The $\mathbf{g}_i$ tensor of an ion is coaxial with its ZFS tensor,[46] but the tensors for the two ions need not share common principal values or orientations. In the proteins studied here, the exchange coupling is ferromagnetic ($J < 0$) with $|J| \ll |D_1|, |D_2|$, and the D_i values are negative and the single-ion $m = \pm 2$ spin states lie lowest. As a result, the ground state of the exchange-coupled diferrous center is a non-Kramers doublet split in zero applied field by an energy within the microwave range, which leaves the center EPR active. The splitting, denoted Δ, is determined by the interplay between the ZFS and exchange interactions; it usually is distributed, reflecting a distribution in the rhombic ZFS terms ($E_i = (D_{yyi} - D_{xxi})/2$; $0 \le E_i/D_i \le 1/3$).[4,5,10-12] Equation 1 includes the hyperfine interaction ($\mathbf{A}_{ij}$) between the electron spins and coupled nuclei; purely nuclear terms (nuclear Zeeman and quadrupole) are discussed below.

Griffith[9] rigorously showed that EPR measurements on an isolated NK doublet can be described by a spin Hamiltonian, $\hat{H}_e$, written in terms of a fictitious electron spin $S = 1/2$ (eq 2).

$$\hat{H}_e = \frac{\tilde{g}_{||}\beta B_z}{h}\hat{S}_z + \Delta\hat{S}_x \quad (2)$$

The splitting of the NK doublet by the energy Δ is incorporated into the second term of $\hat{H}_e$ as an interaction of the fictitious spin with an internal field along the x-axis; the Zeeman interaction of the electron spin with an applied field (magnitude B_o) is given by the first term. The only Zeeman contribution is from the $\hat{S}_z$ component of the fictitious spin and is proportional to the projection of the field along a real-space axis, denoted the z-axis; $B_z = B_o\cos\theta$, where θ is the angle between the z-axis and B_o. Thus, the doublet has a $\tilde{g}$ tensor with axial symmetry where $\tilde{g}_z = \tilde{g}_{||}$ is non-zero, but $\tilde{g}_x = \tilde{g}_y = \tilde{g}_\perp \equiv 0$. The combined action of the applied and "internal" field splits the NK doublet by a frequency ν_e (eq 3), and an EPR signal is seen when ν_e equals the microwave frequency, ν_m.

$$\nu_e = \left[\Delta^2 + \left(\frac{\tilde{g}\beta B_z}{h}\right)^2\right]^{1/2} \quad (3)$$

The orientation of the cluster z-axis within the molecular frame of a dinuclear center has not been discussed previously. For $J/|D_i| < 1$, the situation of interest here, straightforward

(46) Weil, J. A.; Bolton, J. R.; Wertz, J. E. *Electron Paramagnetic Resonance: Elementary Theory and Practical Applications*; John Wiley & Sons, Inc.: New York, 1994.

Scheme 1

$$z = \frac{z_1 + z_2}{|z_1 + z_2|}$$
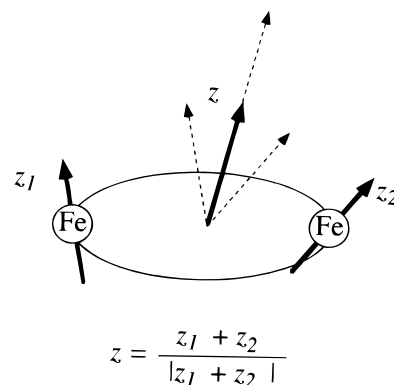
comparison of the matrix elements of eqs 1 and 2 shows that one can write the cluster z-axis unit vector (z) in terms of unit vectors along the tetragonal axes of the two ferrous ions (z_1 and z_2), eq 4a, and can give a companion formula for the cluster g-value ($\tilde{g}_{||}$), eq 4b.[47] Scheme 1 depicts z_1, z_2, and z superimposed on a sketch of the center.

$$z = \frac{z_1 + z_2}{|z_1 + z_2|} \quad (4a)$$

$$\tilde{g}_{||} = (2S_T)g_{||}|z_1 + z_2| \quad (4b)$$

We shall see that NK-ESEEM data can be analyzed to give z, and thereby the z_i. When the two ferromagnetically coupled ions have parallel tetragonal axes (z_i) one gets the well-known relationship for the cluster g-value, $\tilde{g}_{||} = (4S_T)g_{||} \approx 16$ for $S_T = 2$ and $g_{||} \sim 2$.[47] According to eq 4, departures from coaxiality reduce $\tilde{g}_{||}$. This effect presumably plays a major role in determining $\tilde{g}_{||}$, which may be deduced from fitting NK EPR spectra.[10,48]

As an example of the hyperfine interaction, when one nucleus of spin I is coupled to a single iron ion of the center ($\hat{S}_1 \cdot \mathbf{A} \cdot \hat{I}$ as the last term of eq 1), each level of the NK doublet is associated with a $(2I + 1)$-dimension nuclear manifold split by terms that involve the nuclear spin. When the doublet is described by a fictitious spin of $S = 1/2$, the splitting associated with each of the $m_S = \pm 1/2$ spin levels are determined by $\hat{H}_{nuc}$, eq 5,

$$\hat{H}_{nuc} = \tilde{A}_{||}\hat{S}_z\hat{I}_z + \frac{g_N\beta_n}{h}\hat{I}\cdot B_o + \sum_i P_i\hat{I}_i^2 \quad (5)$$

comprised of the electron−nuclear hyperfine coupling and purely nuclear terms, the nuclear-Zeeman, and quadrupole interactions.[46] The hyperfine interaction, the first term of $\hat{H}_{nuc}$, again has a contribution only from the z component of the fictitious spin.[9] The hyperfine parameter in eq 5, $\tilde{A}_{||}$, is proportional to the hyperfine coupling along the interacting ion's crystal-field direction, $A_{||} = |z_1 \cdot \mathbf{A}|$, and to the projection of that direction onto the cluster z-axis, eq 6. The last term in eq 5 describes the nuclear quadrupole interaction; it is diagonal within

(47) One may write a precise formula that allows the two ions to have different g-components along their respective z_i axes, g_{z_1} and g_{z_2}, as well as to have rhombic ZFS tensors with different values of E_i/D_i. Define the vector $Z \equiv [(g_{z_1}\cos\eta_1)z_1 + (g_{z_2}\cos\eta_2)z_2]$, where $\tan 2\eta_i = 2\sqrt{3}(E_i/D_i)$. Then $z = Z/|Z|$ and $\bar{g}_{||} = (2S_T)|Z|$. Note that consistency requires that the vectors z_1 and z_2 be defined so that $z_1 \cdot z_2 \ge 0$. Because $0 \le E_i/D_i \le 1/3$, then, $0.9 \le \cos\eta_i \le 1$, and differences in the rhombicities of the two ions cannot substantially rotate z.

(48) Note that departures from coaxiality diminish the exchange coupling characteristic of a NK doublet where $J/D_i < 1$, with $J_{eff} = (z_1 \cdot z_2)J$.

$$\tilde{A}_{\parallel} = 2S_t A_{\parallel}(z_1 \cdot z) \tag{6}$$

a purely nuclear local frame, and the P_i are its principal components. The middle term is the nuclear Zeeman interaction.

To describe the EPR spectrum of a NK system which shows resolved hyperfine splittings, one can ignore the purely nuclear terms in eq 5. Diagonalization of $\hat{H}_e$ plus the hyperfine term of $\hat{H}_{nuc}$ then gives eq 7 as the resonance condition for a field-

$$\nu_m = \left[\Delta^2 + \left(\frac{\tilde{g}_{\parallel}\beta B_z}{h} + m_I \tilde{A}_{\parallel}\right)^2\right]^{1/2} \tag{7}$$

swept EPR spectrum at fixed microwave frequency, ν_m, where m_I is the nuclear spin projection. This expression predicts an "ordinary" *field-swept* EPR spectrum, with $2I + 1$ hyperfine lines split by $\Delta B = h\tilde{A}_{\parallel}/\tilde{g}_{\parallel}\beta = hA_{\parallel}/g_{\parallel}\beta$.

In contrast to EPR, ENDOR and ESEEM spectroscopies measure so-called ENDOR frequencies, the splittings within the nuclear manifolds at *fixed field*, and here the behavior of a NK system is distinctive. Analysis of the total Hamiltonian, $\hat{H}_t = \hat{H}_e + \hat{H}_{nuc}$, showed[18] that only nuclei with $I \geq 1$ and with significant quadrupole splittings, such as $^{14}N(I=1)$ and possibly $^{17}O(I= 5/2)$ for biomolecules, are likely to give useful NK-ESEEM signals at the low fields under consideration. The deuteron, with $I = 1$ but small P_i, and nuclei with $I = 1/2$ such as ^1H, ^{19}F, and ^{15}N, are not good candidates and the experiments reported here deal solely with ^{14}N. This analysis further showed that for $\tilde{A}_{\parallel} \ll \nu_e$, as applies here, the ENDOR frequencies can be described in terms of a spin Hamiltonian that depends explicitly on the nuclear spin operators and parametrically on m_s. This Hamiltonian, $\hat{H}_{nuc}(m_s)$, eq 8, is the sum of a hyperfine term that involves $\hat{I}_z$, the nuclear spin projection along the cluster z-axis, plus the quadrupole interaction which is best written in terms of operators ($\hat{I}_i$) defined in the coordinate frame that diagonalizes the nuclear quadrupole interaction tensor ($\mathbf{P}$ in eq 5), eq 8a; we consider only applied fields sufficiently low that

$$\hat{H}_{nuc}(m_s) = m_s \tilde{A}_{eff}\hat{I}_z + \sum_i P_i \hat{I}_i^2 \tag{8a}$$

$$= m_s \tilde{A}_{eff} \sum_i (\cos(\alpha_i))\hat{I}_i + \sum_i P_i \hat{I}_i^2 \tag{8b}$$

the nuclear-Zeeman interaction can be ignored. The operator $\hat{I}_z$ also can be defined in the quadrupole frame, eq 8b, in which case the hyperfine term explicitly contains the direction cosines ($\cos \alpha_i$) of the cluster z-axis relative to the quadrupole axes; this dependence on the orientation of z relative to the quadrupole frame is exploited below.[49]

$\hat{H}_{nuc}(m_s)$ is field dependent, even without the nuclear-Zeeman term, because the effective hyperfine coupling, $\tilde{A}_{eff}$, depends on the z-component of the field, (eq 9),[18] where ν_e is given by

$$\tilde{A}_{eff} = \tilde{A}_{\parallel}\left(\frac{\tilde{g}_{\parallel}\beta B_z}{h\nu_e}\right) \tag{9}$$

eq 3. Thus, whereas in a field-swept EPR spectrum the hyperfine splitting for a nucleus coupled to a NK doublet is simply given by the constant $\tilde{A}_{\parallel}/\tilde{g}_{\parallel}\beta = A_{\parallel}/g_{\parallel}\beta$ (eq 7), the

---

(49) The hyperfine interaction also gives an m_s-dependent contribution to the quadrupole term.[18] This term is expected to be small, and we ignore it and discuss only the true quadrupole constants, the P_i. For histidine this term could contribute to line-broadening but is unlikely to be resolved as a splitting around the frequencies determined by the true quadrupole contributions. For azide, the expected magnitude of $A_{\parallel}$ is unknown and the issue is open.
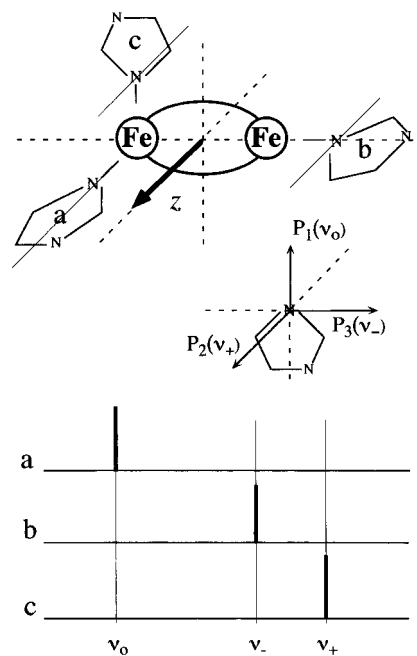

Figure 2. Orientation of ^{14}N quadrupole axes relative to the histidyl plane (center). The orientation was determined from ref 50. Parentheses give the transition observed when B_o is along that axis. Cartoon of the diferrous center with three orthogonal histidyl ligands (top) and idealized zero-field NK-ESEEM frequency-domain spectra for the three ^{14}N ligands (bottom).

hyperfine interaction parameter measured in an ENDOR or ESEEM experiment, $\tilde{A}_{eff}$, depends on B_z.[49] For small B_o this parameter increases linearly with B_o, vanishing in zero field and for orientations where $z \perp B_o$. To illustrate the sharp reduction in the effective hyperfine interaction implicit in eq 9 for the small applied fields employed here ($B_o < 20$ G), eq 10 gives

$$\tilde{A}_{eff}(MHz) \approx A_{\parallel}(MHz)\left(\frac{B_o(G)}{100}\right)\cos \theta \tag{10}$$

as the numerical result for $\tilde{A}_{eff}$, for a nucleus interacting with one ferrous ion of a diiron site in resonance at X band ($\sim$9 GHz).

The P_i in eq 8 are the principal values of the nuclear quadrupole interaction tensor. The tensor is traceless, $P_1 + P_2 + P_3 = 0$, and we choose the three principal components so that $P_1 < P_2 < P_3$. Transitions among the three nuclear levels defined by the quadrupole interaction for $I = 1$ are the three pure nuclear-quadrupole frequencies, defined as ($\bar{\nu}_0 < \bar{\nu}_- < \bar{\nu}_+$), and given by eq 11. For the $^{14}N(I=1)$ of histidine bound

$$\bar{\nu}_+ = \bar{\nu}_{13} = P_3 - P_1$$

$$\bar{\nu}_- = \bar{\nu}_{12} = P_2 - P_1 \tag{11}$$

$$\bar{\nu}_0 = \bar{\nu}_{23} = P_3 - P_2$$

to Fe of ferrimyoglobin, the principal values, $[P_1 < P_2 < P_3]$, are reported to be $[-1.1, +0.3, +0.8]$ MHz, and the orientation of the ^{14}N-quadrupole axes relative to the His molecular frame is given in Figure 2.[50] The quadrupole tensor also is commonly parametrized in terms of $K = |P_1|/2 = e^2qQ/4$ (usual symbols)

---

(50) Scholes, C. P.; Lapidot, A.; Mascarenhas, R.; Inubushi, T.; Isaacson, R. A.; Feher, G. *J. Am. Chem. Soc.* **1982**, *104*, 2724–2735.

Table 1. Pure Quadrupole Data for ^{14}N Bound to the Fe[a]

protein	ν_1 (MHz)	ν_2 (MHz)	ν_3 (MHz)	e^2Qq (MHz)	η
Histidine					
N$_3$Hr$_{red}$	0.43	1.71	2.22	2.62	0.39
		1.89	2.36	2.83	0.33
		2.08	2.36	2.96	0.19
N$_3$R2$_{red}$	0.61		2.23	2.57	0.47
MMOH$_{red}$ (*Mc* and *Mt*)[b]	0.60	1.75	2.33	2.72	0.44
N$_3$Rr$_{red}$ (CRr$_{red}$)[c]	0.45	1.84	2.29	2.75	0.33
Fe^{III}Mb[d]					
PDO[e]				2.2	0.45
Azide[f]					
^{14}N$_3$Hr$_{red}$			2.58		
^{14}N$_3$CR$_{red}$			2.5	2.84	0.20
^{14}N$_3$Rr$_{red}$		1.7, 1.9			

[a] Frequencies are from projections of the field-dependent peak positions back toward $B_o = 0$. [b] Data for *Mc* and *Mt* are indistinguishable. [c] Data for Rr and CRr are indistinguishable. [d] met-myoglobin; ref 50. [e] Phthalate dioxygenase (PDO). Reference 51. [f] As discussed in text, each protein shows only one type of transition, from one or two substates; it is assumed that the quadrupole parameters are the same for the two proteins (see text).

and $\eta = (P_3 - P_2)/|P_1|$; previous values for Fe-bound ^{14}N of imidazole are[50,51] $K \approx 0.55$ MHz and $\eta \approx 0.45$ (Table 1).

For a nucleus with $I = 1$, the Hamiltonian $\hat{H}_{nuc}(m_s)$ can be diagonalized by using published equations (eqs 10 and 11 of ref 45). The resulting energies (but *not* the wave functions) are the same in both electron-spin m_s manifolds, and thus the coupled electron-spin, nuclear-spin system shows three doubly-degenerate ENDOR frequencies for a given orientation. These frequencies depend on the field through the effective hyperfine interaction, $\tilde{A}_{eff}$ (eq 9). They are denoted (ν_+,ν_-,ν_0) because as $B_z \to 0$ the $\tilde{A}_{eff}$ vanishes, $\hat{H}_{nuc}(m_s)$ (eq 8) tends toward the pure quadrupole Hamiltonian, and as a result the nuclear frequencies evolve into the pure quadrupole frequencies, $(\bar{\nu}_+, \bar{\nu}_-, \bar{\nu}_0)$.[49] Such behavior is exhibited explicitly in the field-dependent shifts of the transition frequencies, $\delta\nu_{ij}$, as calculated to second order in the hyperfine interaction. These are given in the Appendix, eq A-12.

The wave functions and transition frequencies for $\hat{H}_{nuc}(m_s)$ have been used to calculate NK ESEEM spectra through incorporation into Mims' well-known density-matrix treatment for the two- and three-pulse echo intensities,[20] which holds for NK,[18] as well as Kramers, systems. The essential features of these spectra are demonstrated by the perturbation calculations of the Appendix, while the exact solutions have been incorporated into a computer program that models NK-ESEEM spectra, as described in the Materials and Methods section. Figure 3 presents the computer-calculated field dependence of the NK-ESEEM frequency-domain spectra for a center that has nuclear parameters (figure legend) relevant to the case of N$_3$Rr$_{red}$ (see below). The $B_o \to 0$ limiting spectra show three peaks centered at the pure quadrupole frequencies. Although the spin–echo modulation (but not the echo itself), and thus the features in the frequency-domain spectrum, vanish *at* zero applied field, such model computer calculations indicate that the pure quadrupole frequencies can be determined reliably by projecting the measured peak frequencies back to zero magnetic field. As the field is increased, the peaks increase sharply in intensity and spread in frequency (eg., eq A-13−16) because of the field dependence of $\tilde{A}_{eff}$ (eq 5). This latter also leads to a shift in the maximum as shown for the ν_+ peak in Figure 3, inset. As the field is further increased the peaks display an asymmetric
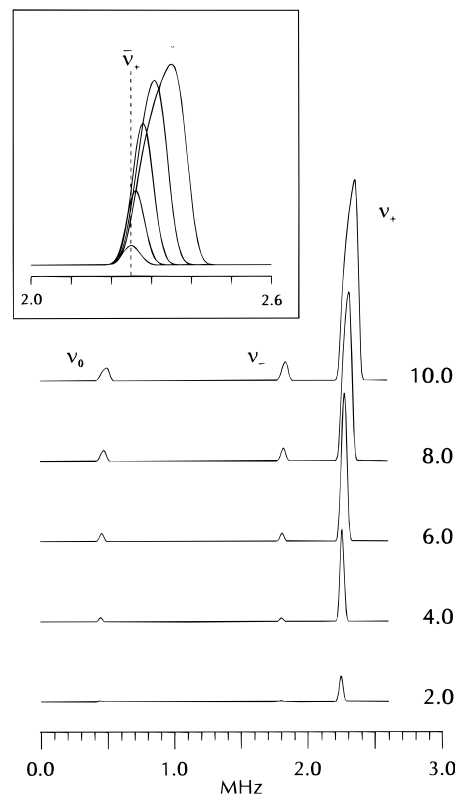
(51) Gurbiel, R. J.; Batie, C. J.; Sivaraja, M.; True, A. E.; Fee, J. A.; Hoffman, B. M.; Ballou, D. P. *Biochemistry* **1989**, *28*, 4861−4871.


Figure 3. Simulated ^{14}N NK-ESEEM frequency-domain spectra for the indicated fields (B_o) calculated as described in the Materials and Methods section for the following parameters: K = 0.675 MHz; η = 0.33; $\cos^2(\alpha_1)$ = 0.030; $\cos^2(\alpha_2)$ = 0.941; $\cos^2(\alpha_3)$ = 0.029; A$_{||}$ = 8 MHz. Inset: Expanded view of the ν_+ peak.

shape as predicted by the perturbation theory (eq A-18). The difference in frequency between the two edges of a feature is governed by the hyperfine coupling, A$_{||}$, and can be used to determine it; in the perturbation treatment this difference is given explicitly by $\delta\nu_{ij}^{max}$ (eq A-12).

The perturbation theory predicts that at low applied fields the intensities depend explicitly on the orientation of the z-axis relative to the quadrupole frame, as given by the $\cos(\alpha_i)$ of eq 8 (see eqs A-15 and A-16). In particular, in the limit where z is along one (k) quadrupole-axis direction, only the (ij) transition appears in the frequency-domain spectrum. This is confirmed by the computer calculations, as illustrated in the frequency-domain spectra of Figure 3. These show that when z is nearly along the P_2 quadrupole-axis direction ($\cos(\alpha_2) \sim 1$), the $\nu_+ = \nu_{13}$ transition is dominant. As a consequence, the relative intensities of the three ^{14}N(I=1) transitions of bound histidine as $B_o \to 0$ provide a means of determining the orientation of the z-axis of a NK metal center relative to the molecular framework of the imidazole plane. As illustrated in Figure 2, the intensity of ν_0 is determined by the projection of z on the nitrogen lone pair (the direction of P_1, the tensor component of largest magnitude); that of ν_+ by the projection on the normal to the imidazole plane (P_2), and that of ν_- by the projection on the in-plane direction normal to the first two (P_3). Figure 2 also depicts a diiron(II) center with three bound imidazoles having different orientations relative to the z-axis of the NK doublet of a reduced diiron center, along with the idealized $B_o \to 0$, pure-quadrupole patterns expected for their individual ESEEM frequency spectra. As we shall see, the difficulty presented by these conclusions is that the spectrum of a center with multiple histidines should be a superposition of their individual spectra.
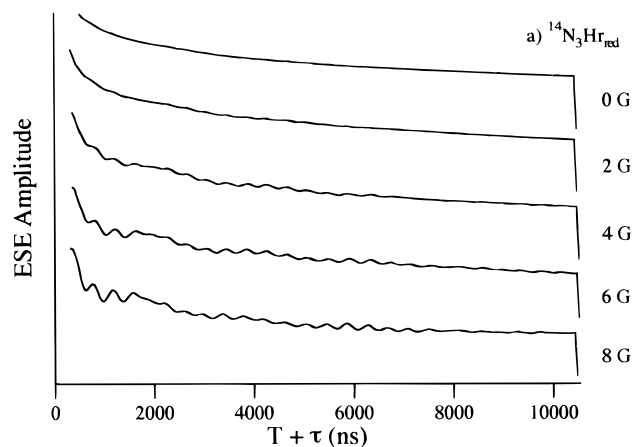
Figure 4. Field dependence of three-pulse ESEEM time waves for $^{14}N_3Hr_{red}$. Conditions: B_o parallel to the microwave magnetic field (B_1); microwave frequency, 9.69 GHz; 100 Hz repetition rate; microwave power ca. 5 W; τ (spacing between the first and second pulses), 140 ns; increment in T (spacing between the second and third pulses), 40 ns; microwave pulse widths, 16 ns; temperature, 2 K.

Results

The integer-spin EPR signals for the diferrous centers of N_3-Hr_{red}, $MMOH_{red}$, N_3R2_{red}, N_3Rr_{red}, and N_3CRr_{red} obtained by conventional X-band (9.5 GHz) cw-EPR measurements each consist of a broad resonance extending from 0 to approximately 1000 G,[10,11,21,28,42] indicating that the NK doublets in these integer-spin systems are split in zero applied field by an amount comparable to the X-band quantum, $\Delta \sim 0.3$ cm^{-1}. In contrast, the same samples generate an observable electron spin−echo only for small values of the magnetic field. Typically, the electron spin−echo amplitude is the largest at $B_o = 0$ and becomes negligible by magnetic field values of 50 to 100 G. This rapid falloff is tentatively associated with the strongly field-dependent spin relaxation seen in the integer-spin EPR,[12] and requires further investigation.

Figure 4 presents the field-dependence of the 3-pulse ESEEM time waves for $^{14}N_3Hr_{red}$; the trends are representative of those seen for all the proteins studied. Although the electron spin−echo amplitude is largest at zero applied field, the echo decays smoothly without nuclear modulation as the interval (T) between the second and third pulses in the 3-pulse echo sequence is increased.[52] A magnetic field of only a few gauss applied parallel to the microwave field, however, introduces nuclear modulation, the depth of which increases rapidly with B_o. Such behavior is completely explained by the theory presented above and in the Appendix. It originates in the field dependence of the electron-nuclear coupling as embodied in the effective hyperfine coupling parameter, $\tilde{A}_{eff}$, eqs 8−10; the origin is made explicit in eqs A 14−16.

Figure 5 compares frequency-domain ESEEM spectra of all proteins studied, as obtained by Fourier transformation of the corresponding time waves collected at fields of ~10 G. As discussed above, for proteins with natural isotopic abundance, ESEEM is expected only from $^{14}N(I=1)$ nuclei with significant couplings, namely, from directly coordinated ^{14}N ligand atoms. The conclusion that the peaks seen for natural-abundance $MMOH_{red}$ preparations come from the ^{14}N of bound histidine was confirmed by the demonstration that the modulation is abolished in protein that is globally labeled with $^{15}N(I=^1/_2)$.[13] For the other proteins studied here azide binding is required to
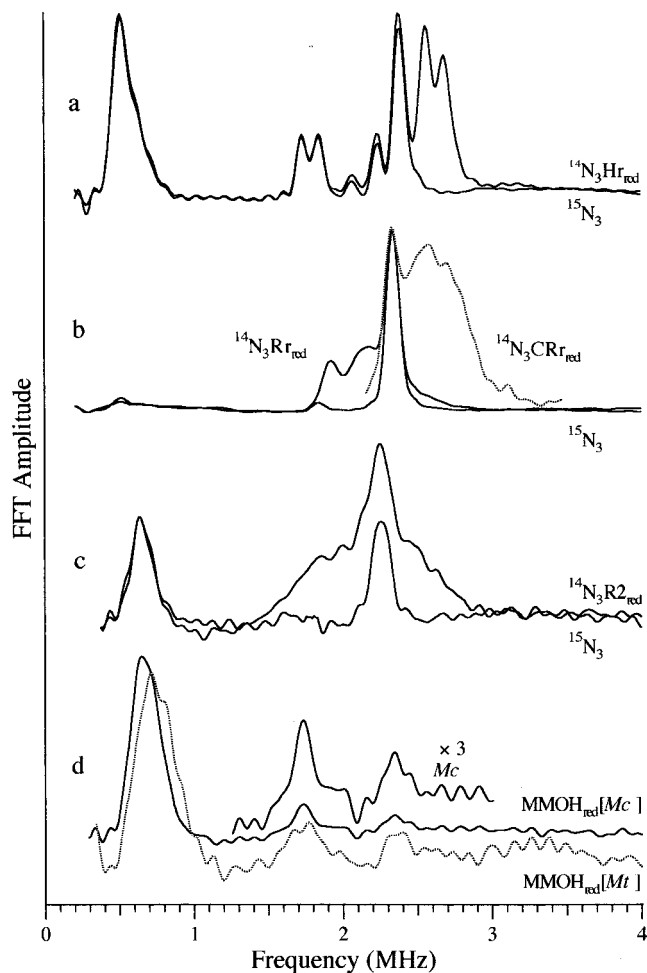
(52) The spectrum denoted $B_o = 0$ was collected with zero *applied* magnetic field. Magnification of this time domain-spectrum reveals shallow modulation resulting from the earth's magnetic field (≈ 0.4 G).
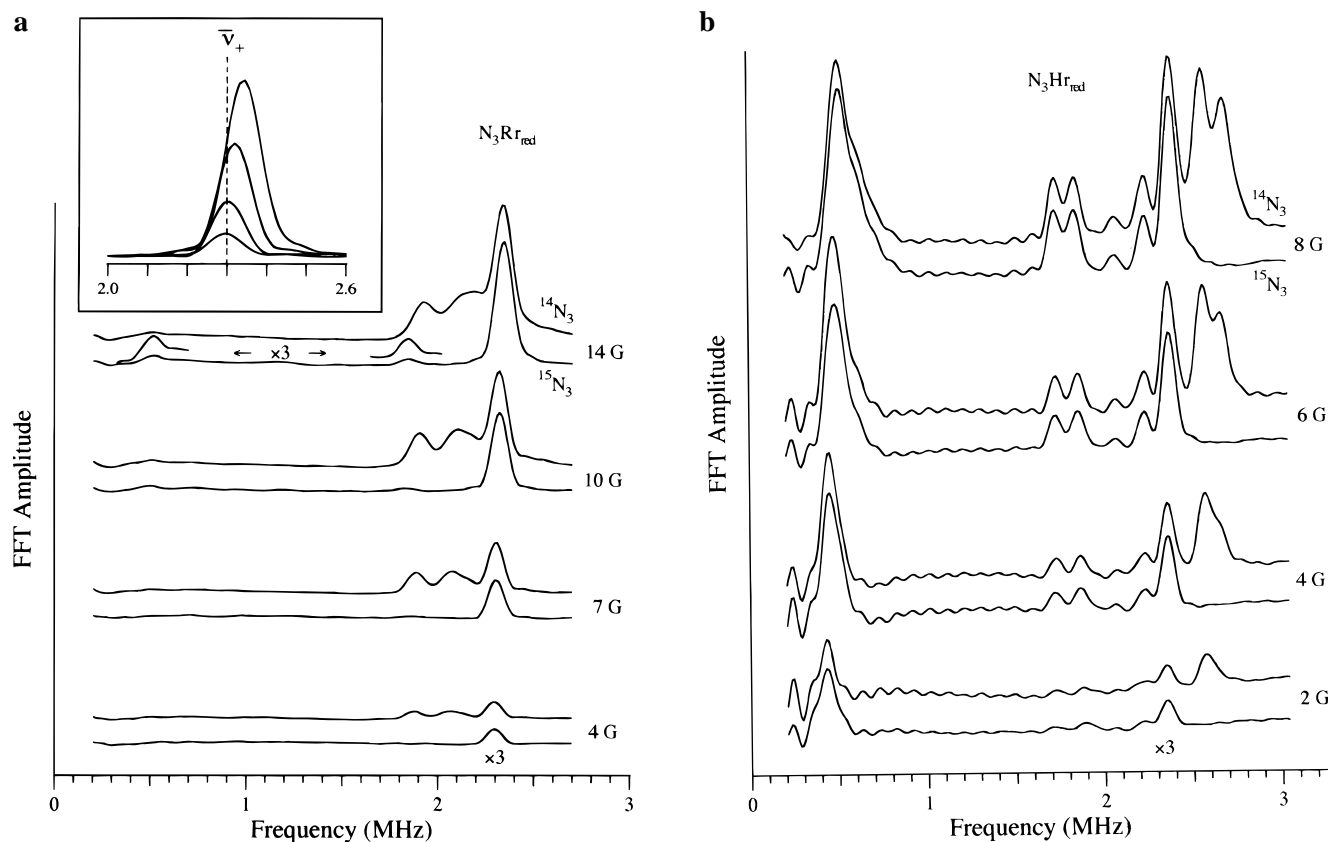

Figure 5. Three-pulse ESEEM frequency domain (ENDOR) spectra. (a) $^{14/15}N_3Hr_{red}$ (8 G); (b) $^{14/15}N_3Rr_{red}$ (10 G) and (broken lines) $^{14}N_3$-CRr_{red} (8 G); (c) $^{14/15}N_3R2_{red}$ (10 G); (d) $MMOH_{red}(Mc)$ (10 G), and MMOHred (*Mt*) (9 G). Conditions: As for Figure 4, except for microwave frequency, 9.49 GHz ($^{14/15}N_3R2_{red}$) and 10.02 GHz (MMO-H_{red}).

generate the ferromagnetic coupling necessary to observe the non-Kramers EPR signal. In these instances the spectra from samples prepared with $^{14}N_3{}^-$ contain peaks from ^{14}N of both azide and histidine, while those from samples with $^{15}N_3$ azide arise solely from histidyl ^{14}N ligands. As can be seen in Figure 5, the frequency components associated with $^{14}N_3$-ligand nitrogens can be identified by comparison of the frequency-domain NK-ESEEM spectra from the $^{14}N_3{}^-$ and $^{15}N_3{}^-$ preparations. To determine the quadrupole frequencies we collected ESEEM data over a range of small applied fields and, as discussed above, projected the measured peak frequencies back to zero magnetic field. Figure 6 presents the data collected for $^{15}N_3Rr_{red}$ and $^{14,15}N_3Hr_{red}$.

Consider first the frequency-domain spectra of $^{15}N_3Rr_{red}$, which consists of three sharp features, an intense high-frequency peak and two weak peaks at lower frequencies (Figures 5 and 6). These are assigned in order of decreasing frequency as the ν_+, ν_-, and ν_0, transitions from bound ^{14}N of histidine. According to the theory, for $B_o \rightarrow 0$ the three peaks for a ^{14}N are centered at the three pure-quadrupole frequencies, but even the low applied fields ($B_o < 20$ G) used here can shift the peaks from the limiting values. Although one edge of a feature remains at the quadrupole frequency, independent of the applied field, the other edge shifts because of the field dependence of the effective hyperfine parameter (see eq A-12); as a result, the peak frequency changes with increasing field (Figure 3). To

a

b

Figure 6. Three-pulse ESEEM frequency-domain (ENDOR) spectra of N_3Rr_{red} and N_3Hr_{red}. Upper and lower traces at each value of B_o are obtained from protein treated with $^{14}N_3^-$ and $^{15}N_3^-$, respectively: (a) $^{14/15}N_3Rr_{red}$ (Inset: expanded view of the ν_+ transition). (b) $^{14/15}N_3Hr_{red}$. The corresponding time waves for $^{14}N_3Hr_{red}$ are presented in Figure 4.

determine the quadrupole frequencies we collected ESEEM data for this sample, and every other, over a range of small applied fields and projected the measured peak frequencies back to zero magnetic field. This type of data is illustrated by Figure 6. The field dependences of the $^{15}N_3Rr_{red}$ experimental spectra, Figure 6a, as well as of the model spectra presented in Figure 3, confirm that as B_o approaches zero the NK-ESEEM peaks go to a well-defined pure-quadrupole frequency. This effect is seen particularly well in the expanded presentations of the ν_+ peak, where for $^{14,15}N_3Rr_{red}$ one finds that $\bar{\nu}_+ = 2.295$ MHz; $\bar{\nu}_-$ and $\bar{\nu}_0$ are similarly obtained from the other two transitions. The three pure-quadrupole frequencies obtained from the spectra are listed in Table 1, and as required obey the sum relationship, $\bar{\nu}_- + \bar{\nu}_0 = \bar{\nu}_+$; they correspond to the following values, $K = 0.64$ and $\eta = 0.47$. The observed shifts with increasing B_o, as well as the concomitant increase in intensity, agree with the expectations of the perturbation approach (eqs A-12 and A-16) and are well reproduced by the computer calculation that employs a value of $A_{||} = 8$ MHz (Figure 3), which is extremely plausible for histidine bound to an iron ion.[50,51,53] Lastly, the area of the intense high-frequency peak for $^{15}N_3Rr_{red}$ appears to be proportional to B_o^2 for B_o up to ~10 G, as predicted by the second-order calculation of the modulation depth (eq A 16). Spectra of $^{15}N_3CRr_{red}$ are indistinguishable from those of $^{15}N_3$-Rr_{red} at all fields.

The ^{14}N-histidyl ν_+ peak for $^{15}N_3Rr(CRr)_{red}$ is *extremely narrow*, with a limiting $B_o \to 0$ G halfwidth of $\delta\nu \lesssim 0.07$ MHz. In fact, this width is determined by the length of the data record (10 μs) plus broadening from the (slow) decay of the modulation in the time domain; the true line width necessarily is much less

than observed. Thus, if two histidines were bound to the diiron center their quadrupole frequencies would have to be almost *precisely* the same (±0.01 -0.02 MHz) to give such sharp lines. Moreover, as illustrated by eq A-16 and Figures 2 and 3, a histidyl ^{14}N NK ESEEM spectrum can have the intensity pattern observed for $^{15}N_3Rr(CRr)_{red}$, with ν_+ dominant, only if the cluster z-axis lies almost exactly normal to the imidazole plane. It is improbable that two histidines could bind to two different iron ions in a nonsymmetrical protein environment, yet display quadrupole frequencies that are so precisely the same and have their planes so closely parallel. Instead, we infer that the spectra of $^{15}N_3Rr$ and $^{15}N_3CRr$ arise from the ^{14}N of a single histidine coordinated to one of the ferrous ions of the diiron center. The X-ray crystal structure of the diferric form of Rr shows only one coordinated histidine, with a second histidine in the vicinity of the cluster, but apparently not coordinated to Fe.[22] The structure invites the question as to whether this second histidine might coordinate in other cluster oxidation states. We interpret the present data to indicate that such is not the case for the azido-diferrous state of Rr or CRr.[54]

The frequency-domain spectra of the two MMOH$_{red}$, *Mc* and *Mt* (Figure 5), are virtually the same, to within the precision allowed by the low modulation amplitudes and low S/N.[13] They show three relatively broad transitions at approximately the same frequencies exhibited by $^{15}N_3Rr_{red}$; these again may be assigned in order of decreasing frequency as the ν_+, ν_-, and ν_0 ^{14}N quadrupole transitions. In this case it is the intensity for ν_0 that is large relative to those of the other two, although the

(53) Iwata, S.; Saynovits, M.; Link, T. A.; Michel, H. *Structure* **1996**, *4*, 567−579.

(54) At minimum, the second histidine must coordinate much more weakly than the first, with a hyperfine coupling so small as to give negligible modulation (eqs 9 and A-16).

intensity differences are not as pronounced as in $^{15}N_3Rr(CRr)_{red}$. Given that the diiron center of MMOH has two histidine ligands, one bound to each Fe, the three peaks are assigned as the sum of spectra from the two coordinated ^{14}N atoms. The breadth of the peaks likely reflects inequalities in quadrupole parameters for the histidines. The equivalent spectroscopic signatures of the two $MMOH_{red}$ proteins in the reduced state, as well as in the mixed-valence state,[17] indicate that they have similar active-site electronic as well as geometric structures. The intensity of the dominant ν_0 peak is dependent on the projection of the cluster z on the nitrogen lone pair, roughly in the direction of the Fe–N bond (eqs A 15, A 16; Figure 2). In the structure of $MMOH_{red}$ the two Fe–N bonds subtend an angle of $\sim 60°$, and model calculations show that the intensity pattern exhibited by $MMOH_{red}$ can be matched if z roughly bisects the angle between the two bonds. We return to this point below.

In contrast, the spectrum of $^{15}N_3R2_{red}$ shows two peaks of similar intensity (Figure 5). Comparing the frequencies of these peaks with those of the other proteins reveals that they should be assigned as ν_+ and ν_0, with ν_- too weak to be detected. The frequencies and derived quadrupole parameters are given in Table 1. The crystal structure of $R2_{red}$ indicates that there are two histidyl ligands to the diiron center,[26] and thus the spectrum in Figure 5 also is a summation. As illustrated in Figure 2, the absence of a ν_- peak from either histidyl ^{14}N shows that the cluster z-axis lies orthogonal to the P_3 axes of both ligands, namely, in the P_1–P_2 planes of the two.

The spectrum of $^{15}N_3Hr_{red}$ displays six transitions that are associated with histidyl ^{14}N and that can be grouped into frequency regions associated with the three quadrupolar transitions (Figure 5). The crystal structure of Hr_{red} shows a total of five histidine ligands, two to one iron and three to the other iron (Figure 1).[23] In N_3Hr_{red} the azide presumably binds to the five-coordinate iron making both iron ions six coordinate. The above discussions emphasize that not all of the quadrupole transitions, ν_+, ν_-, and ν_0, are necessarily observed for a given coordinated nitrogen, and it is clearly impossible to make a unique assignment to all peaks. Nonetheless, by use of the summation relationship for the three quadrupole frequencies of a single type of ^{14}N, $\nu_- + \nu_0 = \nu_+$, we have made tentative assignments of the observed peaks to three distinct types of histidine ligand. The peak frequencies and resulting quadrupole and hyperfine parameters are presented in Table 1.

The spectra of the Fe-bound ^{14}N of azide can be obtained by comparing $^{14,15}N_3$ frequency-domain spectra because the ^{14}N peaks are lost upon incorporation of $^{15}N_3$. As will become clear, it is useful to consider the data for $^{14}N_3Hr_{red}$, $^{14}N_3Rr_{red}$ and $^{14}N_3$-CRr_{red} jointly. In the data for $^{14}N_3Hr_{red}$, at 8 G, Figure 5, one sees two azide $^{14}N_3$ peaks, at $\nu \sim 2.6$–2.7 MHz. As the field is decreased, Figure 6b, these peaks shift slightly, merge, and sharpen, while losing intensity as $B_o \rightarrow 0$. From this behavior one can extrapolate a single limiting $\bar{\nu}$ frequency with good precision. No other $^{14}N_3$ features are discernible to lower frequency. The ^{14}N-azide signal from $^{14}N_3CRr_{red}$ is similar to that of $^{14}N_3Hr_{red}$ (Figure 5), with about the same $\bar{\nu}$ (Table 1). Comparing the $^{14}N_3$ and $^{15}N_3$ data for N_3Rr_{red} (Figures 5 and 6), one instead sees two ^{14}N-azide peaks at frequencies between 1.5 and 2 MHz. Careful examination of this and other spectra discloses no other $^{14}N_3$ peaks to lower or higher frequency. As the field approaches zero the two peaks sharpen as they lose intensity, tending toward limiting peak frequencies of $\bar{\nu} \sim 1.7$ and 1.9 MHz.

These results can be interpreted in several ways that would require very different quadrupole parameters for the ^{14}N of azide

bound in the two proteins. It seems more reasonable to assume provisionally that K and η for Fe-bound azide are roughly the same for all the proteins studied, $^{14}N_3Hr_{red}$, $^{14}N_3Rr_{red}$, and $^{14}N_3$-CRr_{red}. As a result, the ^{14}N-azide intensity near $\nu \sim 2.6$ MHz seen for $^{14}N_3Hr_{red}$ is assigned as ν_+; the splitting at higher fields could reflect two substates of the protein, each having the same values of $\bar{\nu}$ for the azide but with different hyperfine shifts. The ^{14}N-azide peak for $^{14}N_3CRr_{red}$ (Figure 5) is similarly assigned as ν_+, with almost the same value of $\bar{\nu}_+$ (Table 1). The absence of a detectable azide ν_- feature for either protein indicates that the azide is oriented so that z lies approximately normal to P_3 (Figure 2); the failure to see ν_0 could mean either that z is in fact along P_2 or merely that ν_0 is masked by histidyl ν_0 peaks. For $^{14}N_3Rr_{red}$ one can instead assign the azide signal (Figures 5 and 6a) as ν_- for two substates that have ^{14}N-azide with z lying roughly along P_3, rather than P_2. Given that the histidyl-^{14}N pattern is the same in $^{15}N_3Rr_{red}$ and $^{15}N_3CRr_{red}$, the observation of different azide transition for the two proteins, ν_+ for the latter but ν_- for the former, means that their azide ions bind in quite different orientations relative to the cluster core. This difference could involve a large rotation about the Fe–N bond ($\sim 90°$) or even the binding of azide at a different site on the Fe coordination sphere, for example, by displacing a different O of a bidentate carboxylate (cf. Figure 1). Combining the azide $\bar{\nu}_+$ frequency from $^{14}N_3Hr_{red}$ and $^{14}N_3CRr_{red}$ with an average $\bar{\nu}_-$ from $^{14}N_3Rr_{red}$ gives $K \sim 0.71$ MHz and $\eta \sim 0.2$ for ^{14}N of azide bound to Fe^{II} (Table 1). Interestingly, the field-dependent shifts of the azide ν_+ peaks for $^{14}N_3Hr_{red}$ (Figure 6b) and $^{14}N_3CRr_{red}$ (data not shown) are the largest seen to date, and indicate that $A_{||}$ for ^{14}N of azide is more than double the ~ 8 MHz value used to model the behavior for histidine (Figure 3). The azide ^{14}N contribution to the spectrum of $^{14}N_3$-$R2_{red}$, Figure 5, extends over the range of frequencies, ~ 1.5–2.5 MHz, that includes the azide peaks for $^{14}NRr_{red}$ and $^{14}NCRr_{red}$. One possible interpretation of this pattern is that it reflects roughly comparable contributions from the two types of azide orientation seen for $^{14}N_3Hr_{red}$ and $^{14}N_3CRr_{red}$. Given that $^{14}N_3R2_{red}$ was prepared under conditions where one azide binds, not two,[28,42] we dismiss for now the possibility that the pattern arises from two distinct azide ions present simultaneously. Future work on the dependence of the NK-ESEEM results on azide concentration will test this conclusion.

Discussion

This report has extended the theory for ESEEM and ENDOR of NK spin systems[18] to allow direct interpretation of experimental data and has used this theory to compare the ^{14}N ESEEM results from a suite of diferrous carboxylate-bridged proteins. The theory and experiments presented focus on the limit of low applied field. Together they indicate that the primary results of an experiment are as follows: (i) the high-precision determination of nuclear quadrupole coupling parameters for ^{14}N bound to the metal center (Table 1); (ii) the orientation of the cluster z-axis (eq 4) relative to the histidyl ^{14}N quadrupole axes, which knowledge, it will be seen, can be used to determine the orientation of the single-ion tetragonal crystal fields; and (iii) information about conformational effects that perturb bound azide. As a secondary result, one can estimate the ^{14}N hyperfine coupling associated with the projection along the single-ion z-axis (see Figure 3).

The ^{14}N quadrupole-tensor values for the histidyl nitrogens bound to the Fe^{II} ions of the diferrous carboxylate-bridged centers of Rr, CRr, MMOH, and R2 are similar, with $K = e^2qQ/4 \approx 0.68$ MHz and $\eta \approx 0.4$ (Table 1). This value of K is noticeably larger than $K \sim 0.55$ MHz found earlier for histidine

bound to the Fe^{II} ion of the mixed-valence [2Fe−2S] Rieske-type center,[50] which has one other His and two sulfide ligands,[50,53] and to the Fe^{III} ion of ferrimyoglobin, with its highly N-rich coordination.[51] In the case of hemerythrin, it appears that at least one histidyl nitrogen has a similar value of K and η, but at least 2 others appear to show an even larger K ($K \approx$ 0.72 MHz), and a smaller η. The quadrupole parameters are commonly treated as being determined by distribution of the total electron density at N among the three 2p atomic orbitals of N.[55,56] The value of K for the bound ^{14}N of azide is comparable to that for His, but η is much smaller (Table 1). The large value of $A_\parallel$ for bound azide also is of particular interest. To our knowledge, there are no literature values reported for the quadrupole parameters of an azide ^{14}N ion bound to any metal ion, and none for the hyperfine coupling of azide bound to a high-spin ferrous or ferric ion. A deeper understanding of these results will undoubtedly require a broader range of experimental values in conjunction with high-level electronic structure calculations.

The ability to orient the cluster z-axis relative to the ^{14}N histidine quadrupole frame, and thus relative to the crystal structure as in Figure 7, is a qualitatively new feature of these experiments. The striking aspect of the present results is that the cluster z-axis appears to take a well-defined orientation relative to coordinated histidine. This conclusion is obvious in the case of N_3Rr_{red}, where we detect only one histidine ligand to the cluster and the results unambiguously show that z corresponds to the normal to the plane of this His.

To extend this conclusion to clusters with two coordinated histidines we begin by considering $MMOH_{red}$, the only protein studied for which there is an X-ray structure of the precise diferrous state under investigation. Figure 7a superimposes the quadrupole axes for the two N(His) atoms on the diferrous cluster of $MMOH_{red}$. The cluster z is related to the individual ion z_i through eq 4 (Scheme 1). The z_i of a ferrous ion in turn corresponds to the axis of its tetragonal crystal field.[46] We used eq 4 to calculate the cluster z-axis that would arise if the local z_i axes at each ferrous ion lie along (a) the Fe−N(his) bond (resultant denoted ^az); (b) along the normal to the imidazole plane (^bz), and (c) along the in-plane P_3 direction (^cz). Thus, ^az corresponds to the average Fe−N(His) direction and ^bz to the average normal to the His planes, and ^cz is roughly orthogonal to the other two. Calculation of the projections ($\cos(\alpha_i)$; eq 9) of these vectors in the local quadrupole frames shows that the observed NK ESEEM spectra could not arise if either ^bz or ^cz were the cluster z. The vector ^az, however, lies near to the P_1 axis for both histidyl nitrogens ($\alpha_1 \sim 20-30°$) with small components along the other two quadrupole axes for both (Figure 7). This orientation matches the direction of z inferred from the experimental spectra, and model calculations that adopt this vector as z reproduce the experiments (Figure 5) quite well.

The X-ray structures of the azido-diferrous proteins N_3R2_{red} and $N_3Rr(CRr)_{red}$ have not yet been determined. Given that the His ligands have been proposed to act as a structural framework,[26] for heuristic purposes we have superimposed the ^{14}N quadrupole tensor axes on the histidyl nitrogens of the crystal structure of $R2_{red}$[57] and of diferric rubrerythrin, Rr_{ox},[22] Figure 7b,c. As indicated in Figure 2, the absence of a ν_o peak from either histidyl ^{14}N of R2 suggests that the cluster z-axis lies approximately orthogonal to the P_3 axis of both ligands, a direction that corresponds to the cross product of the in-plane

P_3 axes of the histidines. In fact, for $R2_{red}$ the average of the normals to the His planes, ^bz as defined above, is essentially equivalent (parallel) to this vector, and it thus is superimposed on the structure of $R2_{red}$ in Figure 7b. Model NK ESEEM calculations that employ this z agree moderately well with experiment, although they suggest that z lies somewhat farther away from P_2 toward P_1 in the actual azido cluster.

These analyses of NK-ESEEM intensities for diferrous clusters thus support the idea that the direction of the tetragonal ZFS axis of a histidine-bound ferrous ion is fixed by His−Fe bonding, and that the histidines not only provide a structural framework for the cluster but also play a key role in determining the electronic properties of the O_2-activating diferrous state. It appears that the tetragonal ZFS axes lie approximately along the normal to the plane of the His ligand in $N_3Rr(CRr)_{red}$ but roughly along the Fe−N bonds in $MMOH_{red}$; for N_3R2_{red} they take an intermediate orientation, lying in the planes defined by the Fe−N bonds and the histidine normals. Thus, the NK ESEEM experiment on frozen solutions provides an important complement to UV−vis and mcd experiments,[58,59] which give the magnitudes of crystal-field splittings but not their directions.

For N_3Rr_{red}, the very precise orientation of z relative to a ligand of a *single* ferrous ion, as indicated in Figure 7c, in fact presents a puzzle because eq 4 predicts that z should correspond to an average of the z_i directions for *both* ions. It is possible that there is an accidental coincidence of local tetragonal directions. More likely, the assumptions that underlie eq 4 are not valid here because the ZFS tensor of the ferrous ion without a histidyl ligand is very different from that of the one with the His. This conjecture awaits further study of the electronic properties and structure of this protein state. The absence of any difference between the ^{14}N-histidine parameters of N_3Rr_{red} and N_3CRr_{red}, despite the reorientation of azide, might also suggest that in Rr_{red} the azide binds to the ferrous ion that does not coordinate histidine.

Regardless of the above issues, the results for $^{15}N_3Rr_{red}$ and $^{15}N_3CRr_{red}$ clearly show that the formation of CRr by elimination of the 39-residue C-terminal Rr FeS_4 domain, which is remote from the diiron cluster, perturbs neither the histidyl−Fe bonding in Rr nor the orientation of single-ion ZFS tensors as manifest in the orientation of the cluster z relative to histidine. Nonetheless, the native and truncated proteins exhibit different redox potentials,[21] the azide-bound forms show differences in their NK EPR spectra ($g = 19.8$ for N_3Rr_{red} but 17.5 for N_3CRr_{red}),[21] and comparison of the ^{14}N-azide ESEEM for $^{14}N_3Rr_{red}$ and $^{14}N_3$-Crr_{red} shows that the *deletion of the C-terminal domain causes no less than a major reorientation of azide bound to the diferrous cluster*. Rr crystallizes as a tetramer where the subunit interfaces involve the C-terminal domain.[21] Thus, the effects caused by removing this domain could arise from alterations in the interactions between Rr monomers. To the extent that the binding of azide mimics that of dioxygen, such an influence of protein−protein interactions on a ligated diferrous cluster could model a component of the mechanism by which binding of protein B to $MMOH_{red}$ activates the latter for methane oxidation by dioxygen.[27,60] Attempts to test this possibility are underway.

(55) Ashby, C. I.; Cheng, C. P.; Brown, T. L. *J. Am. Chem. Soc.* **1978**, *100*, 6057−6063.

(56) Brown, T. G.; Hoffman, B. M. *Mol. Phys.* **1980**, *39*, 1073−1109.

(57) Logan, D. T.; Su, X.-D.; Åberg, A.; Regnstrom, K.; Hajdu, J.; Eklund, H.; Nordlund, P. *Structure* **1996**, *4*, 1053−1064.

(58) Pulver, S.; Froland, W. A.; Fox, B. G.; Lipscomb, J. D.; Solomon, E. I. *J. Am. Chem. Soc.* **1994**, *116*, 12409−12422.

(59) Solomon, E. I.; Zhang, Y. *Acc. Chem. Res.* **1992**, *25*, 343−352.

(60) Liu, K. E.; Valentine, A. M.; Wang, D.; Huynh, B. H.; Edmondson, D. E.; Salifoglou, A.; Lippard, S. J. *J. Am. Chem. Soc.* **1995**, *117*, 10174−10185.
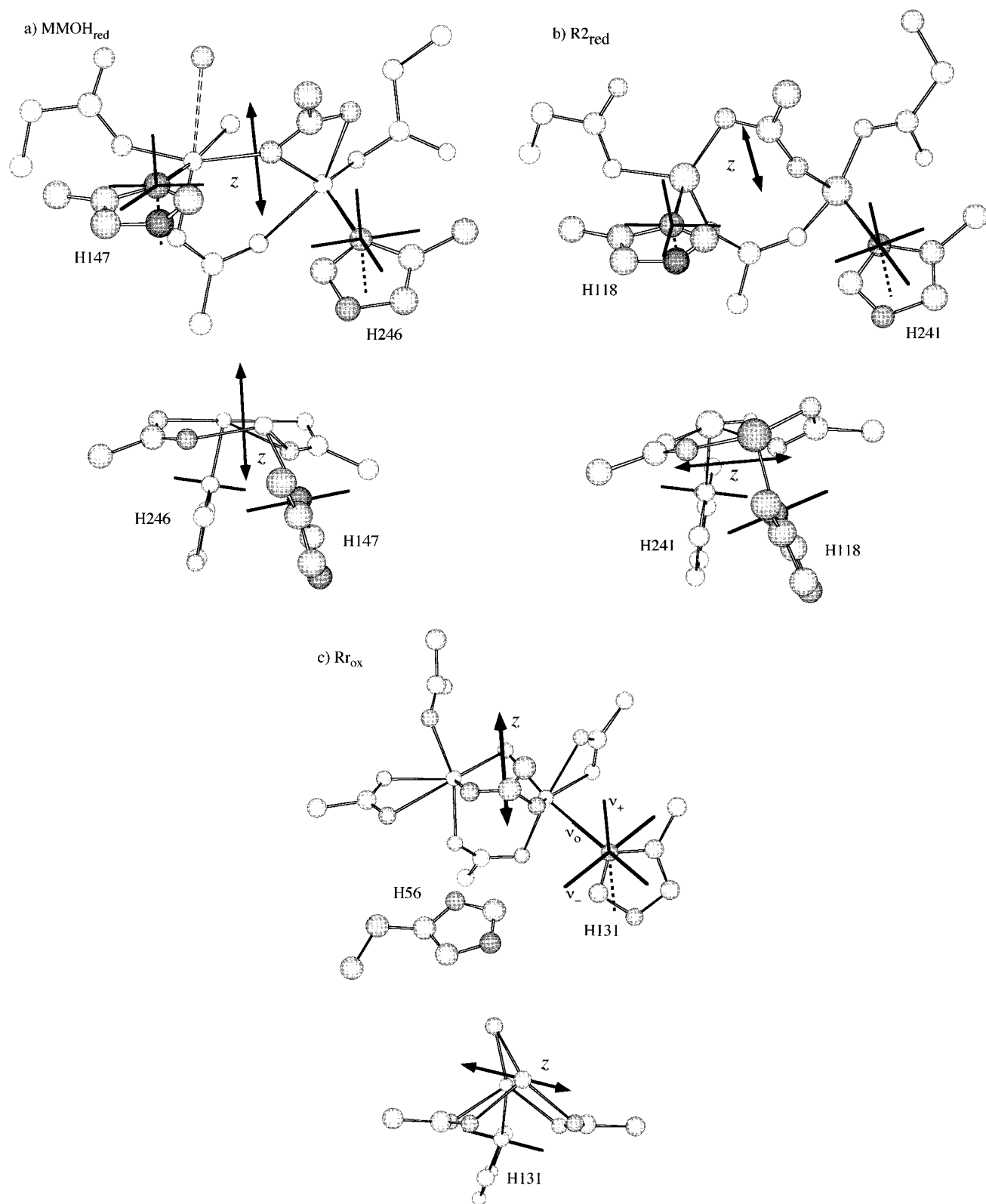
Figure 7. Crystal structures of protein-bound diiron clusters with the ^{14}N quadrupole-tensor axes and proposed cluster z axes superposed. For clarification, compare with Figure 1. In each case, in the upper view the two Fe lie roughly in the plane of the paper; the lower view is rotated to look more nearly down the Fe−Fe direction and retains only bridging ligands and bound His. (a) MMOH$_{red}$(Mc); cluster z is parallel to the average Fe−N(His) vector (eq 2) *and* to the average His normal (P_2). In the lower view, H147 is in front. (b) R2$_{red}$: cluster z is parallel to the cross-product of the P_3 vectors (see Figure 2) for the two histidines. In the lower view H118 is in front; this is the His closest to Y122. (c) Two views of Rr$_{rox}$: cluster z is parallel to the normal of the imidazole plane of the only histidine ligand. In the lower view, H131 is bound to the farther Fe and its β-carbon has been removed.

Appendix: NK ESEEM in Perturbation Theory

   Although our actual NK ESEEM simulations (e.g., Figure 3) employ exact solutions of the Hamiltonian $\hat{H}_{nuc}(m_s)$ (eq 8),

to illustrate the behavior of a NK electron spin interacting with an $I = 1$ nucleus we have derived explicit formulas for the frequency-dependent amplitude-modulation function,[20] $\epsilon(\tau,T)$, using a second-order perturbation treatment.[18] One begins by calculating the field-dependent frequencies of the transitions between nuclear sublevels for $I = 1$ to second order in the hyperfine interaction assuming a rhombic quadrupole tensor. One obtains eq A-12 for the frequency shifts, $\delta\nu_{ij}$, where the

$$\delta\nu_{ij} = \nu_{ij} - \bar{\nu}_{ij} = \left[\sigma_{ij}\left(\frac{\tilde{A}_\|\tilde{g}_\|\beta}{h\nu_e}\right)^2 B_o^2\right]\cos^2\theta$$

$$\equiv \delta\nu_{ij}^{\max}\cos^2\theta \qquad (A-12)$$

coefficients, σ_{ij}, depend both on the pure quadrupole frequencies and on the orientation of the cluster z-axis with respect to the quadrupole frame, namely the $\cos(\alpha_i)$ (eq 21b of ref 18). Thus, the NK ENDOR frequencies shift quadratically with B_o for fixed $\cos\theta$ and vice versa, with the maximum shifts for fixed B_o occurring at $\theta = 0$. The shift coefficients σ_{ij} for ν_- and ν_0 can be either positive or negative, but that for ν_+ is necessarily positive.

The second-order perturbation expression for the modulation depth is given by eq A-13,[61] where terms independent of T have been dropped for clarity and where the sum is taken over the three doubly degenerate transitions between nuclear states i and

$$\epsilon(\tau,T) = \sum_{i<j}^{3\text{tran}}\left[\frac{16}{3}b_{ij}^2(1 - \cos(2\pi\nu_{ij}\tau))\right]\cos(2\pi\nu_{ij}(\tau + T)) \qquad (A-13)$$

j; additional terms would appear in higher order.[49] The modulation function of eq A-13 shows the well-known suppression effect in which the ESEEM by frequencies in one m_s manifold are suppressed frequencies associated with the other manifold.[20] As the ENDOR frequencies associated with the two m_S levels are the same in this instance, each modulation frequency thus is suppressed by itself ("self-suppression") through the T-independent cosine function in eq A-13. The modulation depth parameters, the b_{ij}, have the form exemplified by that for the ν_+ transition ($i = 1, j = 3$), eq A-14, with cyclical

$$\nu_+ = \nu_{13}: \qquad b_{13} \equiv b_+ = \frac{1}{2}\frac{\tilde{A}\text{eff}\cos(\alpha_2)}{P_3 - P_1} = \frac{1}{2}\frac{\tilde{A}\text{eff}\cos(\alpha_2)}{\bar{\nu}_{13}}$$

$$\propto (A_\|\cos(\alpha_2))(B_o\cos\theta) \qquad (A-14)$$

permutation of the indices for the other transitions. Consideration of eq A-14 shows that the modulation vanishes for $\theta = \pi/2$ and as $B_o \to 0$ ($\epsilon \to 1$);[61] the modulation depth parameters increase quadratically with B_o and are maximum for $\theta = 0$, where the EPR intensity maximizes.

For a fixed value of the applied field, eqs A-13 and A-14 apply to a single molecular orientation relative to the field, and it is necessary to extend them to the ESEEM of a frozen solution. As described in Materials and Methods, the fact that Δ for a NK doublet normally is distributed means that for any applied field, B_o, the resonance condition will be satisfied with equal probability by molecules of every orientation (θ), because for each θ there are molecules that exhibit a value of Δ such that ν_e (eq 3) $= \nu_m$. As a result, at field B_o the three ENDOR transitions each will exhibit the full range of frequencies (frequency shifts) predicted by eq A-12: $0 \leq \delta\nu_{ij} = \nu_{ij} \leq \delta\nu_{ij}^{\max}$. In this case it is straightforward to use the perturbation treatment to arrive at a statistical line shape of modulation depth *vs* frequency for the ESEEM frequency-domain spectrum of a powder sample subjected to an external field B_o, as given by the function I (eq A-15).

$$I = \left[(1 - \cos(2\pi\bar{\nu}_{ij}\tau))\left(\left(\frac{\tilde{A}_\|\tilde{g}_\|\beta}{h\nu_e}\right)\cdot\left(\frac{\cos(\alpha_k)}{\tilde{\nu}_{ij}}\right)B_z\right)^2\right]\delta_{ij}^{1/2}$$

$$\delta_{ij}^{1/2} \equiv (\delta\nu_{ij}/\delta\nu_{ij}^{\max})^{1/2}[|\delta\nu_{ij}^{\max}|/\delta\nu_{ij}^{\max}] \qquad (A-15)$$

According to eq A-15,[62] one edge of a peak in the ESEEM frequency-domain spectrum remains fixed at the pure-quadruple frequency, $\bar{\nu}_{ij}$, while intensity grows to high or low frequency depending on the sign of the σ_{ij} coefficient (eq A-12). The "statistical" line shape has a characteristic functional form, $\delta_{ij}^{1/2}$.[63]

To calculate the total area of a peak for a powder sample in applied field B_o, one integrates eq 15 over all values, $0 \leq B_z \leq B_o$. If spectra are properly normalized, the area I_{ij} under peak ν_{ij} in an ENDOR or frequency-domain ESEEM spectrum of a given ^{14}N should increase quadratically with the applied field,[63] and the observed modulation depth will be $^1/_3$ that predicted for the single orientation where $B_z = B_o$, eq A-16.

$$I_{ij} \propto (1 - \cos(2\pi\bar{\nu}_{ij}\tau))\tilde{A}_\|^2\left(\frac{\cos(\alpha_k)}{\bar{\nu}_{ij}}\right)^2\frac{B_o^2}{3} \qquad (A-16)$$

A key feature of eqs A-15 and A-16 is that they explicitly show that the relative intensities of the three quadrupole transitions observed for a ^{14}N($I=1$) can be used to determine the orientation ($\cos(\alpha_k)$) of the cluster z-axis in the coordinate frame of the quadrupole tensor; the other factors depend only on the measured quadrupole transition frequencies ($\bar{\nu}_{ij}$).

(61) This equation corrects a typographical sign error in eq 32 of ref 18. In addition, to obtain a modulation function that is correctly normalized to unity as $(\tau,T) \to 0$ one must normalize the perturbation wave functions, which was not done in eqs 22 and 31 of ref 18. When this is done, the modulation function is normalized and $\epsilon(\tau,T)$ of eq A-13 is augmented by the term, $\chi_o = 1 - (16/3)\sum^{3\text{tran}}b_{ij}^2(1 - \cos(2\pi\bar{\nu}_{ij}\tau))$.

(62) In writing the suppression coefficient as $(1 - \cos(2\pi\bar{\nu}_{ij}\tau))$, we ignore the frequency shifts $\delta\nu_{ij}$ compared to $\bar{\nu}_{ij}$ for the small shifts being considered ($\delta\nu_{ij} \ll \bar{\nu}_{ij}$; especially true for ν_+ and ν_-).

(63) Prediction of actual peak shapes, as in eq A-15, requires correction because the echo intensity depends on the "flip angle" which is proportional to $\delta_{ij}^{1/2}$; it will further require consideration of differential damping of the modulation with shift, as well as actual pulse shape.